Geophys. J. Int. (2006) **167,** 991–1004 doi: 10.1111/j.1365-246X.2006.03118.x

Particulate kinematic simulations of debris avalanches: interpretation of deposits and landslide seismic signals of Mount Saint Helens, 1980 May 18

Steven N. Ward and Simon Day

Institute of Geophysics and Planetary Physics, Earth and Marine Sciences Building, University of California, Santa Cruz, CA 95064 *USA.*
E-mail: ward@es.ucsc.edu

Accepted 2006 June 21. Received 2006 June 12; in original form 2006 March 13

SUMMARY

We construct a new class of granular landslide models in which avalanches are simulated with large numbers of independent particles moving under the influence of topographically derived gravitational and centripetal acceleration. Concurrently, the particles suffer deceleration due to basal and dynamic friction. The novel aspect of the calculation is that complex particle-to-particle interactions, fluctuating basal contacts, and unresolved topographic roughness within and below the deforming flow are mimicked by random perturbations in along-track and cross-slope acceleration. We apply the method to the 1980 May 18 Mount Saint Helens debris avalanche by constraining the initial geometry and structure of the slide mass from geological data, and the initial failure sequence from eyewitness accounts. After tuning coefficients of mechanical friction and random accelerations, the landslide simulation generates a final deposit whose extent, thickness, morphological structure and lithological variation closely replicate those observed. Moreover, the model avalanche is consistent kinematically with mapped patterns of bedrock scouring, deposit superelevation, and net force history implied from seismic records. To be successful, the slide mass must be divided into upper, high-friction and lower, low-friction members. This division corresponds to fresh, water-unsaturated and hydrothermally altered, water-saturated rock units and points to a mechanical explanation of the kinematics of the debris avalanche. Success in reproducing many features of the Mount Saint Helens avalanche indicates that debris-deposit data may be used to determine the kinematic histories of less well-observed landslides.

Key words: debris avalanches, effective friction coefficients, landslides, randomness, volcano lateral collapse.

1 THE IMPORTANCE OF DETERMINING THE KINEMATIC HISTORIES OF LARGE, HIGH-VELOCITY LANDSLIDES

Large, high-velocity landslides, especially the disintegrative rockslides that develop into debris avalanches (sturzstroms) are remarkable geological phenomena. The Elm (Switzerland) landslide of 1881 prompted Heim's (1882, 1932) first scientific study of these events. He documented the ability of high-speed debris avalanches to travel great distances over flat ground and even up opposing slopes. Heim's work set a pattern of combined interpretation of eyewitness accounts with geomorphological and geological studies of landslide deposits. He recognized that landslide kinematics, embodied in their long travel distances, have important implications in defining hazardous zones around potentially unstable rock masses. We know now, as well, that the exceptional velocities of these landslides have hazard implications. In particular, high-velocity landslides that enter water, or are entirely submarine, source locally or regionally damaging tsunamis. Notable examples include the Lituya Bay rockslide of 1958 (Miller 1960) and the 1888 collapse of Ritter Island volcano in Papua New Guinea (Cooke 1981; Johnson 1987). The latter parented tsunami waves with runup heights of several metres, several hundred kilometres away.

2 ROLES OF LANDSLIDE MODELLING IN DETERMINING KINEMATIC HISTORIES

While being especially informative for disintegrative debris avalanches, detailed post-event geological and geomorphological studies inevitably involve a large degree of interpretation to reconstruct the kinematic histories of the slide masses. Usually, scientists call upon landslide models to unify the interpretation of the runout debris and the interactions of the moving landslide with topography.

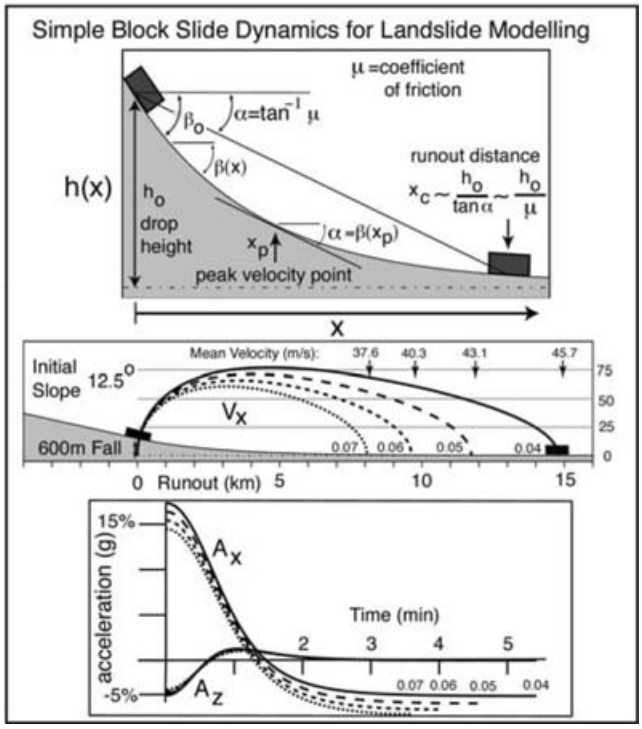

Figure 1. Top panel: simple block-sliding model for landslides. Middle panel: horizontal velocity histories for various sliding distances or coefficients of sliding friction, H/L. Bottom panel: given the shape of the basal surface and a coefficient of sliding friction, an acceleration history—hence equivalent seismic source—can be produced.

Simple block-sliding model. Among his pioneering work, Heim (1882) set a pattern by interpreting large, long-runout and high-speed landslides in terms of a single block sliding down a smoothly decreasing slope while subjected to uniform basal friction (see Fig. 1). This simple block-sliding model continues to be used today to analyse basic landslide features, such as the distance L travelled versus the drop height H of the mass (Heim 1932; Hsu 1975; Ui 1983; Erismann & Abele 2001). The ratio H/L affords a certain insight into the mechanics of landslide motion because, in the simple sliding block model, it corresponds to an effective coefficient of sliding friction μ. Oddly, for many large landslides μ determined by H/L is far smaller ($0.1 < \mu < 0.3$) than experimentally measured μ values for the participating rock types ($0.6 < \mu < 1.0$). Usually too, measured friction values decrease as landslide volume increases. Large submarine landslides and volcano-collapse landslides tend to have the lowest μ values (Ui 1983; Siebert *et al.* 1987; Hampton *et al.* 2002). Amongst non-volcanic subaerial landslides, lower friction values occur in landslides involving porous or poorly consolidated rocks, or where the landslide scrapes up water-saturated river alluvium or sediment during movement (Erismann & Abele 2001). The highest frictional values typify landslides involving low-porosity crystalline basement rocks. The wide range of field-observed μ values and the complexity of lithological and mechanical controls on friction have led to many, sometimes exotic (Shreve 1968) hypotheses for the exceptional mobility of large landslides.

The simple block-sliding model allows easy calculation of velocity histories from the ratio H/L (middle panel of Fig. 1). High velocities and high initial accelerations documented in many landslides bespeak powerful forces exerted by and on the mass as it moves (bottom panel of Fig. 1). Forces transmitted to the Earth from large landslides generate seismic waves that can propagate to great distance. Simple block-sliding models have been employed to calculate dipole-like basal force histories from the acceleration–deceleration phases of historical slides and to compare with the force histories inferred from seismic records (Kanamori & Given 1982; Norris 1994; Brodsky *et al.* 2003).

In part, the longstanding use of the simple sliding block resulted from the difficulty, in the pre-computer era, of quantifying anything more complex. The model has many limitations, however, including the following.

(i) *Limited frictional behaviour.* Simple block-sliding block models accommodate a single basal friction coefficient fixed by a single observable, the ratio H/L. Real debris avalanches suffer both velocity-independent basal friction forces and velocity-dependent drag forces. The relative importance of basal friction and drag forces reflects in the velocity history of the flow, but the eventual runout distance and H/L value may be consistent with a variety of combinations. With multiple friction mechanisms available, landslides may reach their eventual position quickly (high basal friction, low drag) or slowly (low basal friction, high drag). To differentiate the cases, we require other information beyond H/L.

(ii) *Idealized landslide–topography interaction.* Simple block models slide on surfaces with smoothly decreasing slopes. This assumption is too idealized in most real-world applications. Collisions of landslides with steep facing slopes, for instance, can profoundly influence landslide kinematics and seismic force histories. To our advantage, however, careful field observations of landslide–topography interactions can supply much of the 'other information' mentioned in the paragraph above.

(iii) *Inability to transform an initial rock mass to a fragmented, spread-out, and thin sheet of debris.* Use of a single sliding block makes it difficult to directly compare model predictions with debris avalanche deposits, especially where a part of the landslide takes one path and the remaining part of the landslide takes another. Such cases source important data on landslide velocity histories (Plafker & Ericksen 1978; Erismann & Abele 2001). The inability of single sliding blocks to represent the spreading-out of the debris also limits their usefulness in predicting debris avalanche hazardous zones.

First-principle approaches. Certain new landslide models have gone to other extreme of complexity from a simple slide block and attempt to compute landslide motion and deposition from first-principle continuum mechanics. McEwen & Malin (1989) and Sousa & Voight (1995) originally applied first-principle models to volcano-collapse landslides using flows with Bingham rheology. Later applications of this type by Heinrich *et al.* (2001) and Le Friant *et al.* (2003) derive from the velocity and thickness-dependent friction models of Pouliquen (1999) and also include progressive development of full granular flow models by Denlinger & Iverson (2004) and Iverson *et al.* (2004).

Existing first-principle approaches advance simple block models, but they still have a number of problems. First, apart from a thin basal layer, they depth-average the velocity field of the flow on the argument that landslides preserve the stratigraphy of the source rock. Preserved stratigraphy, however, is valid only as a first approximation. Detailed studies (Wadge *et al.* 1995; Glicken 1996; Pollet & Schneider 2004) of landslide deposits show significant shear, fragmentation and lithological mixing on scales of hundreds of metres to kilometres. Linked to the depth-averaging problem is the inability of first-principle models to accommodate spatial or temporal variation of the properties of the landslide mass. Without

analysing deformation within the slide mass, these models cannot include fragmentation and material property changes in a mechanistic fashion.

In the long term, first-principle models may well address the mechanics of landslide movement. Large hurdles exist, however, in the specification of slide-fragmentation behaviour, pore water distribution and hydrogeological characteristics of the failing rock mass. The specification of these features at real-world scales represents an additional set of difficulties in data collection yet to be addressed systematically (Day 1996; Elsworth & Day 1999).

Our approach. In this paper, we develop a new class of granular landslide models that obviate most of the limitations of the simple block-sliding model while maintaining the ease of calculation lost in first-principle approaches. Avalanches are simulated with large numbers of independent particles moving under the influence of topographically derived gravitational and centripetal acceleration. Concurrently, the particles suffer deceleration due to basal (velocity-independent) and dynamic drag (velocity-dependent) friction. The novel aspect of the calculation is that complex particle-to-particle interactions, fluctuating basal contacts, and unresolved topographic roughness within and below the deforming flow are mimicked by random perturbations in along-track and cross-slope acceleration. By this technique, we can integrate geological data on the initial and final state of the landslide mass with eyewitness and seismic constraints.

3 OBSERVATIONAL CONSTRAINTS ON THE MOUNT SAINT HELENS DEBRIS AVALANCHE

Both direct and indirect observations constrain the kinematic histories of large long-runout landslides. Key aspects include: (i) reconstruction of the pre-collapse geology of the failed rock mass; (ii) volume, distribution and morphological differentiation of the deposit; (iii) interaction of landslides with topography; (iv) lithological zonation; (v) eyewitness observations; and (vi) seismological constraints.

(i) *Reconstruction of the pre-collapse geology of the failed rock mass.* Where a rock mass was lithologically differentiated prior to failure (e.g. through the presence of distinct volcanic units or of intrusions), it is possible to determine which parts of the rock mass ended up where in the final deposit. Further, the physical nature of the different units helps in the assignment of rock mechanical parameters, spatially within the pre-collapse mass.

At Mount Saint Helens, the key distinction in the pre-collapse stratigraphy defined by C.A. Hopson (see fig. 2 of Glicken 1996) is between the upper Andesite–Basalt unit (relatively fresh to fumarolically altered, dark reddish or purplish at outcrop) and the lower Older Dacite unit (more or less hydrothermally altered at low temperatures and pale grey at outcrop). Clasts and blocks of these units are easily identified and mapped in the field. The rock alteration patterns (Pevear *et al.* 1982; Glicken 1996) suggest that the Andesite–Basalt unit sat largely above the pre-1980 water table, while the Older Dacite unit was largely water saturated and subject to long-term hydrothermal alteration that reduced both strength and permeability. Glicken (1996) also mapped other minor units of the pre-collapse stratigraphy as lithologies in the landslide deposit, including the younger dacites of the Goat Rocks and Summit domes. Masses of younger dacites intermingle within areas dominated by the Andesite–Basalt units (Glicken's 'undifferentiated modern unit') and do not appear to have behaved differently from them in mechanics of movement. We reduce the pre-collapse stratigraphy to two units (Fig. 2), each of which forms almost exactly 50 per cent of the landslide mass (Glicken 1996, especially table 2).

(ii) *Volume, distribution and morphological differentiation of the deposit.* The maximum, average, and range of material transport distances, drop heights and spreading extent of the landslide during transport are critical elements for fixing landslide model parameters.

At Mount Saint Helens, Glicken (1996) estimated a total deposit volume of 2.5 km^3 spread over an area of 64 km^2. Distal deposits ran 29 km from the volcano as measured along the axis of the main landslide path north and west from the collapse scar, and dropped 1300 m measured from the approximate centre of the failed rock mass. Because most material came to rest close to the collapse, the centre of mass of the deposit travelled <10 km and dropped some 1000 m. About $\sim$20 per cent of total slide volume travelled past the slope break near Maratta Creek (Fig. 3).

Glicken (1996) particularly emphasized the differentiation of the deposit into two morphological facies. First, a block-rich facies with abundant large ($\sim$100 m) debris avalanche blocks, thick (50–170 m) and concentrated close to the volcano in the North Fork Toutle River valley and its tributary valleys, but spreading up on to adjacent ridges (Fig. 4). The block-rich facies is composed of material that stopped soon after descending the slope of the volcano and being deflected to east or west by interaction with Johnston Ridge,

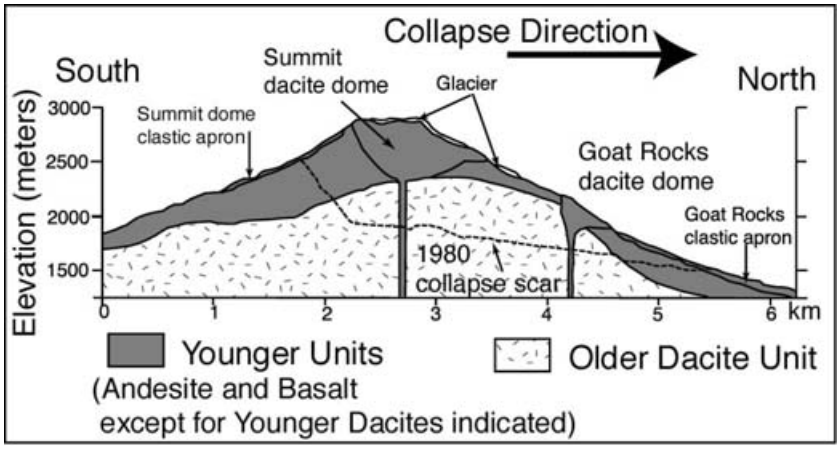

Figure 2. Simplified north–south cross-section of pre-collapse Mount Saint Helens along the axis of the collapse structure: modified after Glicken (1996). Geology of the pre-collapse Mount Saint Helens is dominated by the upper Andesite–Basalt unit and the lower Older–Dacite Unit.

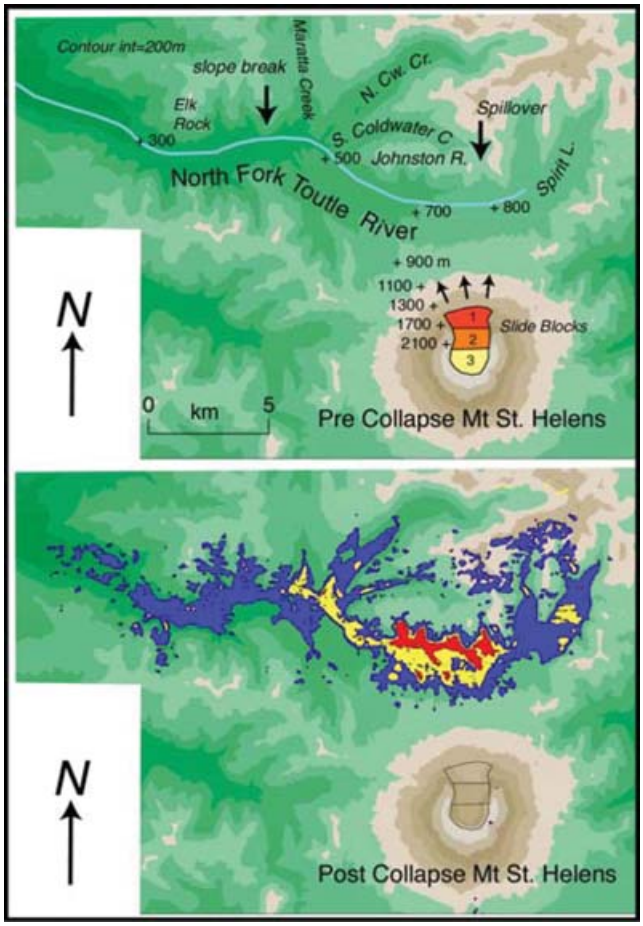

Figure 3. Top panel: Mount Saint Helens vicinity. Colours and labels indicate the three slide blocks that initially accelerated northwards towards Johnston Ridge. Bottom panel: deposit distribution and thickness as measured by pre- and post-DEMs (contours 10, 50 and 90 m). Note decrease in thickness at slope break.

although a part ascended to the crest of the ridge. Blocks of this facies came to rest on slopes as steep as 10°–15° on valley sides. The second morphological facies is mixed or matrix rich, thin (10–40 m) with few large blocks, that extends 12 km down the North Fork Toutle River beyond Maratta Creek but is confined to the valley floor. The matrix-rich facies terminated in a tangled mass of tree trunks and scraped-up debris that may have prevented the unit from running further to the west. The boundary between the block-rich and matrix-rich facies occurs at a constriction in the valley just west of Maratta Creek (Fig. 4). The matrix-rich facies represents only 18 per cent of the total deposit volume (Glicken 1996) but nearly half of deposit extent along the line of maximum travel from the volcano.

Like the situation at Mount Saint Helens, landslide deposits typically contain abundant block-rich units proximally and more matrix-rich deposits at distance. Such morphological differentiation points to internal heterogeneity within landslides. Many studies of debris avalanches generated by volcano collapses have emphasized morphological differentiation of deposits (Wadge *et al.* 1995; Glicken 1996; Belousov *et al.* 1999). Moreover, studies of a number of non-volcanic landslides have also emphasized the changing nature of the deposits versus distance from their source (Laberg & Vorren 2000; Hampton *et al.* 2002; Normark *et al.* 2004; Pollet & Schneider 2004). Glicken (1996) and Pollet & Schneider (2004) explicitly related morphological differentiation to progressive fragmentation and ultimately to changes in material properties during landslide motion.

Morphological differentiation of landslide deposits bears on kinematic modelling strategies because it indicates differences in transport mechanism. These differences may develop progressively, accompanying the gradual fragmentation of the moving slide mass; or, differences in transport mechanisms may exist at the outset, being a property of rock types themselves.

(iii) *Interaction of landslides with topography.* This is revealed both through the geometries of the final deposits and through areas of scouring and non-deposition where landslide debris first ascended and then descended slopes without stopping (Plafker & Ericksen 1978; Evans *et al.* 1989). Landslide–topography interaction, through interconversion of kinetic and potential energy, tells much about landslide velocities. The top panel of Fig. 5 shows the velocity history of a simple sliding block, like that of Fig. 1, the only difference being that the block impacts a steep-faced side wall after sliding about 7 km. At this point, the block suffers sudden horizontal and vertical accelerations (bottom panel, Fig. 5), quite distinct from the simple block-sliding model (Fig. 1, bottom panel).

Mount Saint Helens provides a spectacular example of landslide–topography interaction in the collision of the debris avalanche with the ∼400 m high, steep (mostly > 40°) southern face of Johnston ridge. The collision deflected most of the northward-moving landslide material either eastwards, into Spirit Lake, or westwards down the valley of the North Fork Toutle River. A significant fraction of the landslide also overrode Johnston ridge (Fig. 6a) and descended into the valley of South Coldwater Creek scouring its slopes (Lipman & Mullineaux 1981; Fisher *et al.* 1987). Apart from a few remnant blocks within slumped blast deposits in the floor of South Coldwater Creek, debris that overran the ridge deposited only on a narrow strip of flat ground at the ridge crest and on level ground in the headwaters of the creek (Fisher *et al.* 1987).

Significant block deposition also occurred at the east end of Johnston Ridge (the 'spillover', Glicken 1996) on its relatively gentle southern facing slope (Fig. 6b). West of the spillover, some material seems to have stopped on the steeper slopes of the south face of Johnston Ridge and then slid back down into the North Fork Toutle River valley (Glicken 1996). Blocks originating from the upper part of the pre-collapse stratigraphy stopped at higher elevations and on steeper slopes than blocks from the lower part that returned down to the valley axis.

To surmount Johnston Ridge and enter Coldwater Creek, material must have been travelling at 50–70 m s^{-1} (Voight *et al.* 1983) at the foot of the mountain. These high velocities contrast the 20 m s^{-1} speeds later in debris avalanche movement as implied by the limited superelevation of the matrix-rich facies deposits at bends in the river valley to the west (Voight *et al.* 1983). The separation of the landslide into a smaller fraction that did surmount the ridge and a larger proportion that did not, indicates substantial velocity variation within the debris avalanche as it reached the foot of Mount Saint Helens and crossed the Toutle River's North Fork.

(iv) *Lithological zonation.* Where the pre-collapse geology of the source is both known and varied, determining which parts of the rock mass ended up where yields important information. Specifically, the degree of mixing within the moving landslide and whether the sequence of initial rock mass failure was progressive or complex can be gleaned by field mapping (Glicken 1996) or by remote sensing (Wadge *et al.* 1995).

The overall lithological zonation of the Mount Saint Helens deposit (Fig. 4) reveals itself in the impressive colour contrast between

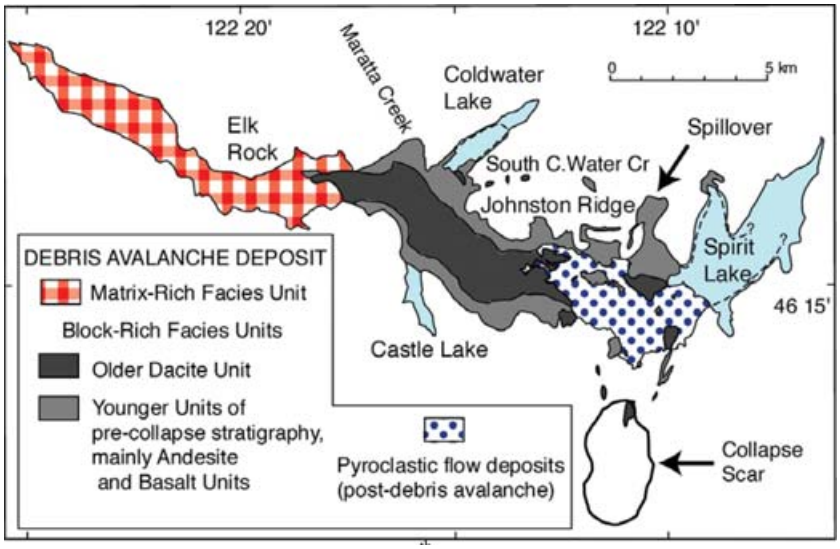

Figure 4. Simplified lithological map of the 1980 May 18 debris avalanche deposit and near-vent pyroclastic flows (after Glicken 1996), showing subdivision of the 1980 debris avalanche deposit according to whether dominant lithology in the deposit originated from upper or lower part of pre-collapse stratigraphy (Fig. 2). Cover of lahars and blast deposit omitted.

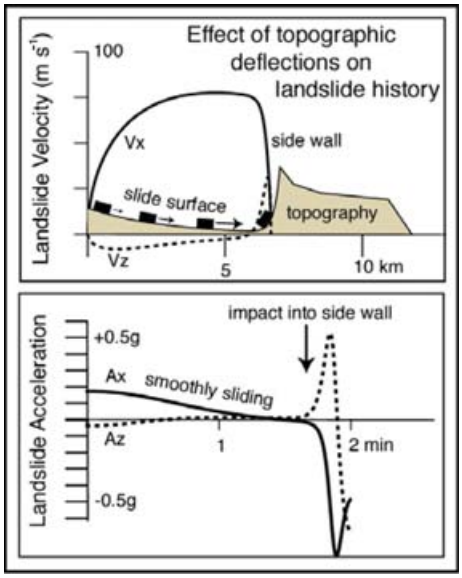

Figure 5. Effect of steep face collision on landslide kinematics. Top panel: velocities versus distance. Bottom panel: accelerations versus time. Contrast Fig. 1.

the Andesite–Basalt unit and the Older Dacite unit. In this landslide, lithological and morphological zonations closely correspond. The Andesite–Basalt unit, along with the Younger Dacite units, now form much of the Block-Rick facies east of Maratta creek. These units fill the floor of the North Fork Toutle River valley and extend up on to its gentler slopes most notably in the 'spillover' south of the head of South Coldwater Creek (Fig. 6b). A distinctive pale-grey lobe of Older Dacite debris avalanche blocks occupies the centre of the North Fork Toutle River and overlies Andesite–Basalt unit blocks. Here, the stratigraphy of the deposit is inverted relative to the stratigraphy of the pre-collapse volcano. Apparently, Older Dacite debris emplaced after the Andesite–Basalt material.

To the west, beyond the break in slope near Maratta Creek that marks the transition between the block-rich and matrix-rich facies, the deposit is more lithologically mixed. Glicken (1996), based on excavations in elevated hummocks accessibly exposed in the early 1980s, considered the matrix-rich facies to be mixed lithologically in proportions comparable to the pre-collapse sequence as a whole. Subsequent incision of the river through the matrix-rich deposit in the Elk Rock reach has exposed largely altered Older Dacite material with rare and distinctive Andesite–Basalt blocks (Fig. 6c) and mixed units rich in the same lithologies. These more cohesive blocks and mixed units form higher ground along the rim of the incised river channel. The hummocks accessible to Glicken before incision of the river were therefore likely comprised of units enriched in Andesite–Basalt and surficial blast deposit material that sedimented on to the moving debris avalanche compared to the bulk composition of the matrix-rich facies. This led Glicken to interpret the matrix-rich facies deposit as being composed primarily of Block 3 material (see discussion below). Recognizing the abundance of altered dacite material exposed in the bluffs created by incision of the river since Glicken's fieldwork, we associate the proximal block-rich unit with the upper Andesite–Basalt (plus younger dacite lava domes) part of the pre-collapse stratigraphy, and more far-travelled matrix-rich units with the lower Older Dacite half of the pre-collapse stratigraphy.

(v) *Eyewitness observations.* The 1980 May 18 landslide of Mount Saint Helens occurred in daylight and in clear weather. Eyewitnesses have well established the initial successive failure of two large and initially coherent blocks (Block 1 and Block 2, Fig. 3) some 30 s apart, and the acceleration of these blocks to $\sim$70 m s^{-1} down the north flank of Mount Saint Helens during the first 70 s of the landslide (Voight 1981). Later photographs in the sequence taken by G. Rosenquist (Voight 1981) document the onset of fragmentation of these blocks into a debris avalanche. After 70 s or so, an expanding blast cloud overtook the leading blocks descending into the valley and obscured further landslide motion. A particular area of uncertainty is the failure and movement history of the so-called 'Block 3' that consisted of the remainder of the eventual landslide mass upslope of Blocks 1 and 2 (Voight 1981; Glicken 1996). Block 3 may have failed progressively or in a piecemeal fashion, producing a long 'tail' to the landslide.

(a)

(b)

(c)

Figure 6. (a) View north and east from Johnston Ridge showing pale bedrock exposed by scouring effect of debris avalanche material as it descended into South Coldwater Creek, and localized deposition of debris avalanche blocks on flat ground at head of creek. Photo courtesy: Eli Silver. (b) View of the 'Spillover' area at the eastern end of Johnston Ridge, with abundant purplish-grey, dark debris avalanche blocks composed of Andesite–Basalt unit material. Photo courtesy: Eli Silver. (c) View of bluff exposing pale-grey Older Dacite unit debris and (at right-hand side) isolated block of Andesite–Basalt unit material, formed by incision of North Fork Toutle River into matrix-rich facies deposit, Elk Rock reach. Photo courtesy: Lee Murai.

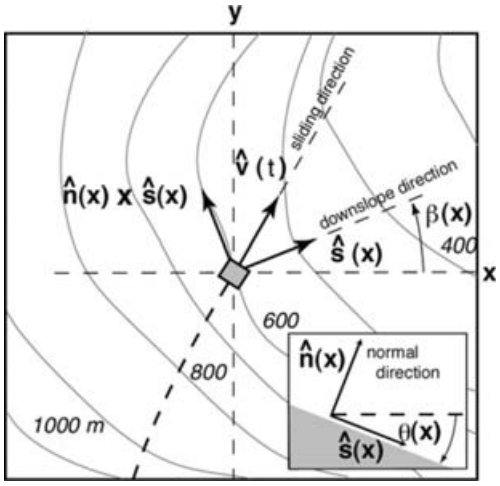

Figure 7. Snapshot of an isolated sliding block. The forces on the block are in the downslope direction, in the direction of sliding $\hat{\mathbf{v}}(\mathbf{x})$, and in the direction normal to the surface $\hat{\mathbf{n}}(\mathbf{x})$.

(vi) *Seismological constraints.* The Mount Saint Helens landslide is notable for the number and quality of seismic signals recorded both locally and at teleseismic distances. By analysing horizontal-component teleseismic records around 250 s period, Kanamori & Given (1982) and Brodsky *et al.* (2003) generated an acceleration history of the landslide. Brodsky *et al.* (2003) interpreted this history in terms of frictional deceleration and obtained an apparent coefficient of basal friction. Their interpretation, however, neglects the topographic interaction of the landslide with Johnston Ridge. Slamming into the ridge likely had more influence on arresting landslide motion in the north–south direction than did basal friction. Kanamori & Given (1982) noted higher-frequency energy in the north–south components of the seismic records about 2 min after the start of the landslide that may have been produced by this collision. After the collision, landslide material travelled both east and west, so net accelerations would have been substantially smaller and more variable than those during the pre-collision phase. Regional and local seismic records interpreted as containing shorter-period landslide signals lasting as long as 10 min bear out continuing accelerations of landslide material over time- and length-scales too small to generate long-period seismic waves (Malone *et al.* 1981; Voight *et al.* 1983; Burger & Langston 1985).

4 RANDOM WALK LANDSLIDE MODEL: MATHEMATICAL CONCEPT

As described above, the 1980 May 18 collapse of Mount Saint Helens is the most intensely observed and studied large landslide in history. This event therefore represents a key test of any landslide simulation. Previous modelling attempts have only been partly successful (McEwen & Malin 1989; Sousa & Voight 1995). No one has attempted to satisfy quantitatively both seismic (force history) and geological (deposit distribution and characteristics) constraints. To do so, we must develop a comprehensive landslide model, yet one that does not out-strip available data.

Sliding blocks revisited. Consider a small sliding block at position $\mathbf{x}(t)$ with velocity $\mathbf{v}(t)$ (Fig. 7). Our approach to modelling its motions views the acceleration of the block's centre of mass to be

$$\begin{aligned}\mathbf{a}(t) &= [\mathbf{g} \bullet \hat{\mathbf{s}}(\mathbf{x}(t))]\hat{\mathbf{s}}(\mathbf{x}(t)) + v^2(t)K(t)\hat{\mathbf{n}}(\mathbf{x}(t)) \\ &\quad + \mu[\mathbf{g} \bullet \hat{\mathbf{n}}(\mathbf{x}(t)) - v^2(t)K(t)]\hat{\mathbf{v}}(t) - \nu[v^2(t)]\hat{\mathbf{v}}(t) \\ &= \mathbf{g} + [\mathbf{g} \bullet \hat{\mathbf{n}}(\mathbf{x}(t)) - v^2(t)K(t)][\mu\hat{\mathbf{v}}(t) - \hat{\mathbf{n}}(\mathbf{x}(t))] - \nu[v^2(t)]\hat{\mathbf{v}}(t)\end{aligned} \tag{1a,b}$$

with $K(t) = -[\hat{\mathbf{v}}(t)\hat{\mathbf{v}}(t) : \nabla\hat{\mathbf{n}}(\mathbf{x}(t))]$. In (1), $\mathbf{g}$ is the acceleration of gravity, $\hat{\mathbf{s}}(\mathbf{x})$ is the downslope direction, $\hat{\mathbf{n}}(\mathbf{x})$ is the unit normal vector upward from the surface, and μ and ν are constant coefficients of sliding and dynamic drag friction, respectively. Often, the dynamic drag coefficient is non-dimensionalized by dividing the last term by some spatial dimension of the block (see Harbitz 1992). The four terms in eq. (1a) represent the downslope gravitational acceleration, the centripetal acceleration due to the along-track curvature of the surface $K(t)$ {i.e. surface curvature in $[\hat{\mathbf{n}}(\mathbf{x}),\ \hat{\mathbf{v}}(\mathbf{x})]$ plane} and the two along-track frictional decelerations. The first, third and fourth terms act tangent to the surface at $\mathbf{x}\,(t)$, while the second term acts normal to it. The centripetal acceleration assures that block velocity stays tangent to the surface. Note from eq. (1b) that if at anytime $\mathbf{g} \bullet \hat{\mathbf{n}}(\mathbf{x}(t)) = v^2(t)K(t)$, an isolated particle could lose surface contact and become airborne. We suppose, however, that as part of a larger granular mass, particles always obey eq. (1b) and follow the topography.

Let the $\hat{\mathbf{x}}$ and $\hat{\mathbf{y}}$ directions be east and north in the horizontal plane and $\hat{\mathbf{z}}$ be up so $\mathbf{g} = -g\hat{\mathbf{z}}$. If $\beta(\mathbf{x}(t))$ is the azimuth of $\hat{\mathbf{s}}(\mathbf{x}(t))$ measured from $\hat{\mathbf{x}}$ towards $\hat{\mathbf{y}}$ in the horizontal plane and $\theta(\mathbf{x})$ is the slope angle reckoned positive downwards (see inset, Fig. 7), then the downslope unit vector is

$$\hat{\mathbf{s}}(\mathbf{x}(t)) = \cos\theta(\mathbf{x}(t))[\hat{\mathbf{x}}\cos\beta(\mathbf{x}(t)) + \hat{\mathbf{y}}\sin\beta(\mathbf{x}(t))] - \sin\theta(\mathbf{x}(t))\hat{\mathbf{z}}. \tag{2}$$

Given a topography, initial block position and velocity, and the friction coefficients, eqs (1) and (2) can be integrated to map block trajectory (see Appendix A). The seismic signature of this sliding block is obtained by applying to the Earth's surface an external travelling force

$$\mathbf{F}_{\text{seis}}(\mathbf{x}(t), t) = -M\mathbf{a}(t), \tag{3}$$

where M is the mass of the small block. [Note, the seismic source description of landslides is not unique. Dahlen (1993) has shown that, to a good approximation, the seismic radiation from external surface force (3) is equivalent to that radiated by certain indigenous dislocation sources.] Using eq. (3) as a seismic source, synthetic waveforms can be generated with regional or global seismic wave propagation codes. To simulate a Mount Saint Helens collapse, many thousands of blocks need to be tracked simultaneously over complex topography and eq. (3) summed over all block positions and each time. In real cases, you might imagine that landslide seismic sources will be complicated functions as they include evolving landslide shapes, reflection of material from topography, potential variations in frictional properties, as well as progressive deposition of material from the moving debris avalanche.

4.1 Introducing random components of motion to simulate particle interactions

Equations like (1) and (2) have found wide success in modelling landslides and debris flows. The 2-D version of these equations with $\nu = 0$, $K(t) = 0$ applied to a smoothly decreasing slope is, in fact, the simple block-sliding model discussed earlier. We propose that multiple independent integrations of the single block equations can better mimic granular landslides if they incorporate elements of randomness. In particular, let eqs (1a) and (2) become

$$\begin{aligned}\mathbf{a}(t) &= [\mathbf{g} \bullet \hat{\mathbf{s}}(\mathbf{x}(t))]\hat{\chi}_s(\mathbf{x}(t)) + v^2(t)K(t)\hat{\mathbf{n}}(\mathbf{x}(t)) \\ &\quad + \chi_\mu[\mathbf{g} \bullet \hat{\mathbf{n}}(\mathbf{x}(t)) - v^2(t)K(t)]\hat{\mathbf{v}}(t) - \nu[v^2(t)]\hat{\mathbf{v}}(t)\end{aligned} \tag{4}$$

and

$$\hat{\chi}_s(\mathbf{x}(t)) = \cos\theta(\mathbf{x}(t))[\hat{\mathbf{x}}\cos\chi_\beta(\mathbf{x}(t)) + \hat{\mathbf{y}}\sin\chi_\beta(\mathbf{x}(t))] - \sin\theta(\mathbf{x}(t))\hat{\mathbf{z}}, \tag{5}$$

respectively, where χ_μ and χ_β are now unitless independent random variables that take on different values every Δt seconds during sliding. Naturally, the expected values of χ_μ and χ_β equal μ and $\beta(\mathbf{x}\,(t))$ such that the average acceleration predicted from eqs (4) and (5) equals that from eqs (1) and (2).

The χ_β function: χ_β introduces random lateral deflections of slide particles from the downslope direction $\beta\,(\mathbf{x})$. Our concept of the physics of granular sliding is that deflections to the right-hand and left-hand sides of the downslope direction given by our model topography occur due to both: random variations in the real downhill direction compared to the model topography, and random cross-slope deflections caused by interparticle collisions. We imagine that either source generates deflections of equal likelihood towards the right-hand or left-hand side or the likelihood of deflection decreases with magnitude of deflection. Let us take a zero mean normal distribution to describe χ_β, that is, the probability of χ_β taking the angle a about model downslope direction $\beta\,(\mathbf{x})$ is

$$\begin{aligned}P[\chi_\beta = a] &= N(a : \beta(\mathbf{x}), \sigma_\beta) \\ &= (\sqrt{2\pi}\sigma_\beta)^{-1} e^{-[a-\beta(\mathbf{x})]^2/2\sigma_\beta^2}.\end{aligned} \tag{6}$$

The χ_μ function: χ_μ introduces random accelerations of landslide particles in the direction of motion. We envision that forward random accelerations stem from three processes

$$\chi_\mu = \chi_\mu^{(1)} + \chi_\mu^{(2)}. \tag{7}$$

Like χ_β, $\chi_\mu^{(1)}$ characterizes the combination of along-track particle collisions (i) among themselves and (ii) with unresolved topographic variations on the basal surface. Both mechanisms sometimes increase speed in the slide direction and sometimes decrease speed in the slide direction. The forward component of randomness would, like the lateral component (6), have zero mean and decrease in likelihood with increasing perturbation. The normal distribution is a sensible choice for $\chi_\mu^{(1)}$:

$$P\left[\chi_\mu^{(1)} = a\right] = N\left(a : 0, \sigma_\mu^{(1)}\mu\right). \tag{8}$$

Potentially, experiments might show eqs (6) and (8) to be closely related functions with randomness due to particle collisions among themselves and with unresolved topographic variations being equal in forward and lateral directions.

The third element $\chi_\mu^{(2)}$ characterizes additional forward randomness due to variations in basal friction as the block speeds downslope. It is this process that causes sliding granular piles to stretch out more in the forward direction than in lateral directions. Because basal friction can only decrease slide speed in the direction of propagation, $\chi_\mu^{(2)}$ can only take on positive values. Recall too that the mean value of eq. (7) must equal μ so with (8), the mean of $\chi_\mu^{(2)}$ must equal μ. One physical interpretation of random basal friction supposes that $\chi_\mu^{(2)}$ can only take the values $\chi_\mu^{(2)} = 0$ or $\chi_\mu^{(2)} = \mu/\psi = \mu_p$ like

$$\begin{aligned}P\left[\chi_\mu^{(2)} = 0\right] &= 1 - \psi, \\ P\left[\chi_\mu^{(2)} = \mu_p\right] &= \psi,\end{aligned} \tag{9}$$

where $0 < \psi < 1$. The random aspect of eq. (9) is that slide blocks have only $\psi \times 100$ per cent of their time or basal area in direct contact with the surface below. For these brief intervals and selected locations, basal friction is very large—$1/\psi$ times the mean value for the slide as a whole. The standard deviation of eq. (9) is

$$\sigma\left[\chi_\mu^{(2)}\right] = \sigma_\mu^{(2)}\mu = \mu[\psi^{-1} - 1]^{1/2},$$

so physical parameter ψ could be estimated from measured $\sigma_\mu^{(2)}$. In sum, however, eq. (10) has mean equal to μ and standard deviation

$$\begin{aligned}\sigma[\chi_\mu] &= \sigma_\mu \mu \\ &= \left[\left[\sigma_\mu^{(1)}\right]^2 + \left[\sigma_\mu^{(2)}\right]^2\right]^{1/2} \mu,\end{aligned} \tag{10}$$

so increases in forward randomness $\sigma_\mu^{(1)}$ trade off with decreases in basal friction randomness $\sigma_\mu^{(2)}$. Outside laboratory experiments, the two processes will be difficult to resolve separately. Given this, a simpler tack here replaces the two distributions (8) and (9) with a normal distribution shifted to μ:

$$P[\chi_\mu = a] = N(a : \mu, \sigma_\mu \mu). \tag{11}$$

Formulation (11) has the advantage of having only one parameter, but it loses the distinction between randomness due to forward particle interaction and randomness due to basal friction variations and the potential to attach physical interpretations to the latter.

Sample landslide models. Fig. 8 illustrates the effects of cross-slope and forward randomness on a simple landslide. In each case, 300 particles initially confined in a square, run down a slope that grades to flat. Each row in the panels shows the granular slide mass at uniformly increasing time steps. In the upper panel, eq. (4) is integrated with σ_β, and σ_μ set to zero. With no randomness on the uniform slope, all of the slide particles experience equal forces and move in a block-like fashion. Only at the slope break does the slide experience slight deformations. In the middle panel of Fig. 8, the along-track variance increases. Now particles experience random forward accelerations and the slide mass stretches out. Randomness parameter σ_μ can be interpreted as an along-track diffusion coefficient (Lima *et al.* 2000). In particular, along-track stretching of a simulated granular pile sliding on a level surface follows like $\sigma_{\text{pile}}(t) \sim \mu g \sigma_\mu \sqrt{t^3 \Delta t/3}$ where Δt is the interval at which the random friction variables in (4) and (5) take on new values. Thus, the fixed quantity of physical interest is $\sigma_\mu \sqrt{\Delta t}$.

In the bottom panel of Fig. 8, cross-slope randomness σ_β is set to 30° while $\sigma_\mu = 0$. Predominantly, the slide mass diffuses laterally. With both forward and cross-slope randomness active in Fig. 9, realistic looking slide distributions result both in map view and cross-section. Comparisons of models with laboratory experiments (Savage & Hutter 1989; Fritz 2002) that launch piles of granular material and measure the evolution of slide shape during motion suggest that $\sqrt{\Delta t}\sigma_\mu = 1 \sim 2\,s^{1/2}$ and $\sqrt{\Delta t}\sigma_\beta = 30^\circ \sim 40^\circ\, s^{1/2}$. Based on these experiments, $\sqrt{\Delta t}\sigma_\mu = 1 s^{1/2}$ and $\sqrt{\Delta t}\sigma_\beta = 30^\circ\, s^{1/2}$ are fixed through the calculation below.

5 APPLICATION: MOUNT SAINT HELENS 1980 MAY 18 COLLAPSE, LANDSLIDE AND SEISMIC SOURCE

5.1 Model setup

Our Mount Saint Helens landslide model time steps equations (4) and (5) at 1 s intervals and tracks 3000 particles. Three thousand keeps the calculation within 'laptop computer' scale, but sufficient to sample landslide behaviour well. Given the total slide volume of $2.5 \times 10^9\,\text{m}^3$, each particle has a $dv = 8.3 \times 10^5\,\text{m}^3$ volume equivalent—roughly a cube 100 m on a side. Consistent with the reconstruction of the pre-collapse volcano and the estimate of the relative volumes of the initial slide blocks, we divide the initial slide mass into Blocks 1, 2 and 3 (Fig. 3, top panel) in the relative volumes of 32, 25 and 43 per cent (Table 1), respectively. Each block is further divided into equal-volume upper and lower sections corresponding to the Andesite–Basalt/Younger Dacite unit and the Older Dacite unit, respectively. We allow the upper and lower units to have possibly different basal friction values.

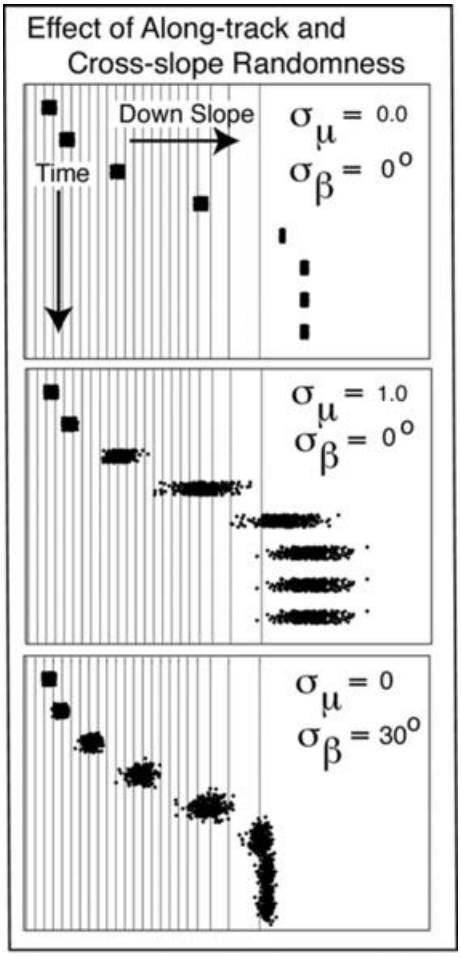

Figure 8. Granular slide model with different choices of along-track and cross-slope randomness. The panels have $\sigma_\mu = 0\ \sigma_b = 0^\circ$ (no randomness), $\sigma_\mu = 1\ \sigma_b = 0^\circ$ (along-track randomness only), and $\sigma_\mu = 0\ \sigma_b = 30^\circ$ (cross slope randomness only).

As dictated by the eyewitness observations, particles in Blocks 1, 2 and 3 were released en-mass at 30 s intervals and allowed to run down pre-eruption topography outside the cavity. Inside the cavity, since neither the pre- nor post-topography suitably describes a basal sliding surface, we took the downslope direction from post-topography, but fixed the slope angles according to unit and block. Within the cavity, all upper unit particles slid on 30° slopes and lower unit particles slid on slopes of 15°, 20° or 25° depending on if they currently occupied the area of Block 1, 2 or 3. This arrangement gives the upper units a greater effective fall height than lower units as required to produce the rapid accelerations of the slide masses seen in the Rosenquist photographs (Voight 1981). (The

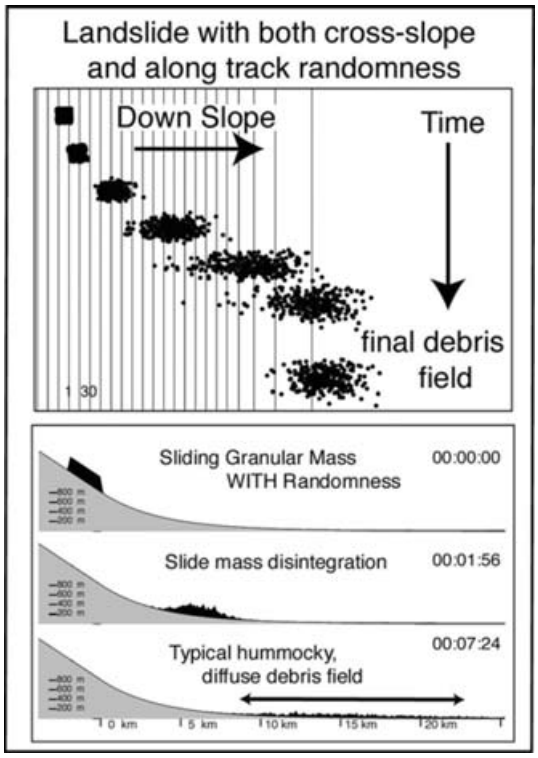

Figure 9. Granular slide model with both along-track and cross-slope randomness. $\sigma_\mu = 1$ and $\sigma_\beta = 30^\circ$ (top panel). Map view (bottom panel) cross-section. Randomness makes realistic looking deposit distributions.

particles could be given an initial velocity to account for high-pressure gasses driving the blocks from behind, but this did not seem necessary.) Centripetal accelerations were turned off for particles in the cavity.

Frictional sliding dictates that when a particle slows below a certain critical speed, basal friction transitions from a low dynamic value to a high static value that eventually freezes the particle in place. A velocity-weakening friction law characterizes the transition. These friction laws can be as complicated as you wish. We assume a one-parameter step function transition at a small fraction of the peak slide speed, 0.5 m s^{-1}, in this case. Smaller critical speeds extend the life of a sliding particle for a few extra seconds, but the particle usually ends up nearby because it is moving slowly near the end. When a new particle stops, its volume dv is flattened over an area according to a Gaussian distribution with width $\Delta =$ 250 m. Specifically, for each particle stopped at $\mathbf{r}_s$, the elevation at $\mathbf{r}$ is increased by

$$\Delta T(\mathbf{r}) = \frac{dv}{\pi\Delta^2} e^{-(|\mathbf{r}-\mathbf{r}_s|/\Delta)^2},$$

topographic slopes and curvatures are recomputed (Appendix A), and those particles still moving slide over the updated surface. Stopped material thus becomes part of an evolving topography that influences the paths of later passing material. Dams, levees and ponded debris lakes form by this process. Apart from interaction with the topography generated by stopped bits of the slide, all 3000 particles run independently with communications among themselves being simulated by the random walk parameters $\sigma_\mu =$ 1 and $\sigma_\beta = 30^\circ$ for $\Delta t = 1$ s.

Given the setup above, only the dynamic drag and basal friction coefficients remain to be set. Unlike Heim's simple block-sliding model, when multiple friction mechanisms are available, their effects can be difficult to untangle from deposit distribution alone (Fig. 10). Fortunately, in the case of Mount Saint Helens, the effects of basal and dynamic drag friction largely separate in time. Because dynamic drag friction dominates during the initial high-speed part of the slide, and basal friction dominates in the later slow moving periods, the observations outlined in Section 3 provide fairly tight constraints on frictional parameters. First, with basal friction initially set to zero, the dynamic drag friction coefficient was selected such that an appropriate fraction of slide material crosses up and over Johnston Ridge. Because the landslide must speed >50 m s^{-1} to overtop the Ridge, values of dynamic drag friction cannot exceed $\nu = 1.3 \times 10^{-4}$ m^{-1}. Secondly, with the dynamic drag coefficient thus set, we adjusted the basal coefficients over several runs. Key constraints were that the upper unit confines itself to the east of the slope break, while enough of the lower unit passed onwards to satisfy the observation that ~20 per cent of total slide volume travelled westwards past the slope break. Basal friction coefficients of 0.05 and 0.0015, respectively, for the upper and lower units fit the bill. One plausible physical explanation for the contrasting frictional values is that pore fluid pressurization on the basal surfaces of the water-saturated lower units gives them lower frictional resistance than the water-unsaturated upper units (Hubbert & Rubey 1959). The concept of friction reduction by interstitial water within landslides is longstanding (see review in Erismann & Abele 2001, pp. 204–228) and finds support in the exceptionally low H/L values associated with landslide passage over water-saturated substrates (Erismann & Abele 2001).

5.2 Model products

Fig. 11 shows four frames from the Mount Saint Helens landslide simulation. (Quicktime movies are available on the Worldwide Web. See Appendix II.) In Panel A, 45 s after the start of the collapse, Block 1 is sliding and spreading downhill. Block 2 has just begun to move and deform, whereas Block 3 remains at rest. This situation corresponds to photograph *o* of the Rosenquist sequence (Voight 1981), some 15 s after the start of movement of Block 2.

Two minutes and fifteen seconds after the start of the collapse (Panel B), most of Block 1 has impacted Johnston Ridge and begun to slide back down the slope and spread laterally. These behaviours

Table 1. Parameters for the Mount Saint Helens landslide model.

	Fractional volume (per cent)	Release time (s)		Basal friction μ	Dynamic friction ν (1/m)	$\sigma_\mu\sqrt{\Delta t}$	$\sigma_\beta\sqrt{\Delta t}$
Block 1	32	0	Upper unit	0.05	0.000 13	$1.0s^{1/2}$	$30^\circ s^{1/2}$
			Lower unit	0.015			
Block 2	25	30	Upper unit	0.05			
			Lower unit	0.015			
Block 3	43	60	Upper unit	0.05			
			Lower unit	0.015			

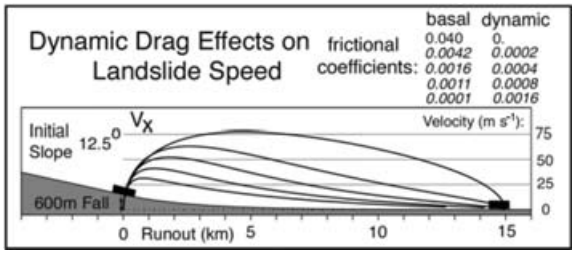

Figure 10. Velocity and position histories of a single sliding-block model with both basal and dynamic drag friction. Several combinations of frictional values may produce the same final block position. Specifically, the block might run rapidly or slowly depending on the ratio of dynamic drag to basal friction.

agree with extrapolated events seen in the Rosenquist photographs (Voight 1981), the lithological distribution of the deposit, and the reversal of the net acceleration inferred from the long-period seismic record. At this time, the faster-moving bits of Block 2 and Block 3 overtake Block 1 particles slowed by the ridge, consistent with the sequence of deposition of these materials on and near the ridge (Fisher *et al.* 1987). Meanwhile, other parts of Block 3 have not yet left the collapse scar, consistent with the failure history inferred for this block. Up to now, particle velocities had been high (50–70 m s^{-1}) and landslide motions controlled by the initial drop height (upper units of the pre-collapse volcano tend to be travelling faster) and the velocity-dependent dynamic drag friction. However, around the time of Panel B, effects of basal friction begin to show. Some of the upper part of the pre-collapse stratigraphy now comes to rest on the crest of Johnston Ridge and at the head of South Coldwater Creek. Parts from the lower units that also passed over the ridge, due to their lower basal friction, continue down the creek, scouring the creek walls in the real case.

After 5 min (panel C), portions of Blocks 2 and 3 have passed over the eastern end of Johnston Ridge and are moving down South Coldwater Creek. Vanguards of the main landslide approach the constriction near the confluence of the North Fork Toutle and North Coldwater valleys. Recall that here, the change in deposit thickness and the block-rich to matrix-rich facies boundary occur. By now many of the high basal friction particles originating high in the pre-collapse stratigraphy have come to rest, whilst the low-friction particles from low in the pre-collapse stratigraphy are still moving. This mechanism inverts the stratigraphy by placing Lower Dacite rich material over Andesite–Basalt material in the axial lobe of the block-rich facies.

Those particles moving after 8 min drain from the main landslide and from South Coldwater Creek and migrate slowly westwards (panel D). These particles are mainly from the lower sections of Blocks 1–3, consistent with the Older Dacite-rich nature of the deposit now seen in the bluffs incised by the North Fork Toutle River (Fig. 6b) and with the low abundance of Younger Dacite clasts from the Summit Dome evident in the matrix-rich facies. At this stage, most Block 3 particles reside east of the constriction, reflecting their delayed start. After 28 min, the leading particles approach the westernmost tip of the observed deposit. Few particles run past here. The ∼30 min duration of model landslide motion exceeds the 8–10 min duration estimated from seismic data (Malone *et al.* 1981; Voight *et al.* 1983; Glicken 1996). Still, there were no direct observations of the debris avalanche or of the subsequent lahars until at least two hours after the initial collapse. Slow motion of a small volume of low-friction material to 30 min cannot be excluded based on eyewitness data. Too, the longer the duration of debris motion,

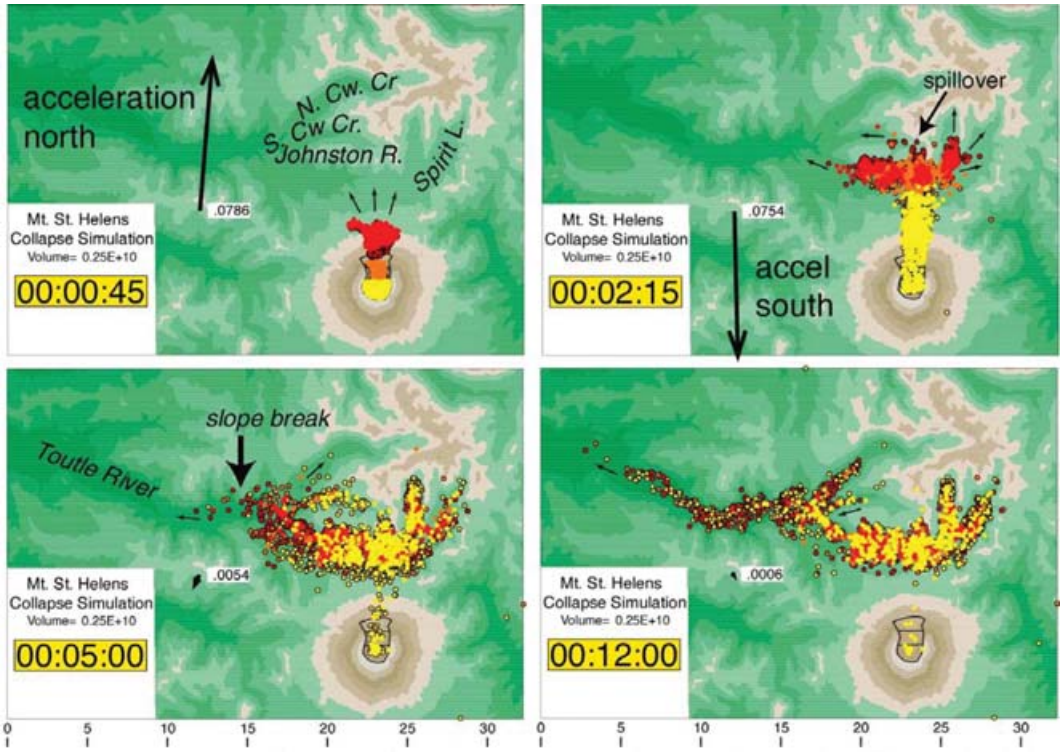

Figure 11. Four frames from a Mount Saint Helens landslide simulation http://es.ucsc.edu/∼ward/msh_colors.mov. Red, orange and yellow denote particles slide Blocks 1, 2, and 3. Particles with dark edges are from the lower units. Dark arrow shows the net acceleration of the landslide in units of g. Note the change in direction of the force in the first $2\frac{1}{4}$ min as material rebounds off of Johnston Ridge.

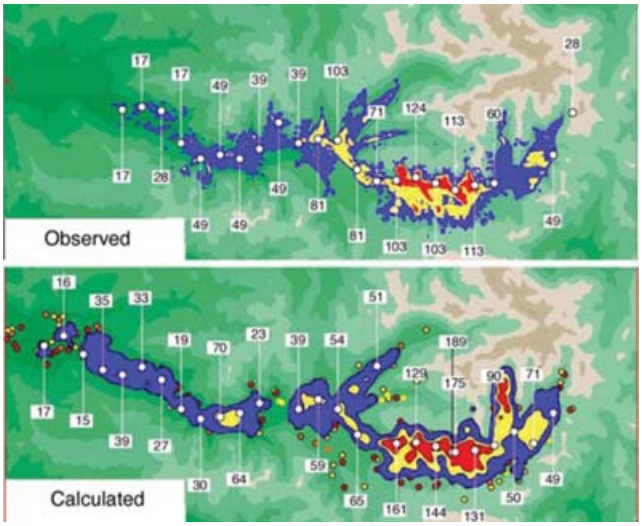

Figure 12. Top panel: observed deposit thickness in metres as determined from pre- and post-digital topography. Bottom panel: computed deposit thickness from the model of Fig. 11. Thickest landslide deposits (∼150 m) are found directly in front of the collapse scar.

the greater potential it has to incorporate juvenile clast-rich material sedimenting out of the blast cloud. A long duration of debris motion provides an alternative explanation for the locally high, but variable, concentrations of juvenile material found in the matrix-rich deposit.

Fig. 12 compares observed and model deposit distribution and thickness. As does the observed deposit, the thickest model deposits concentrate on the northern side of the North Fork Toutle River Valley and exceed 150 m directly in front of the volcano. The model also packs thick deposits on the spillover at the eastern end of Johnston Ridge where the avalanche was funnelled by the canyon walls and on the level ground at the top of South Coldwater Creek, but only minimal deposits in Creek itself. In agreement with field data, significant model deposits extend up the floor of North Coldwater Creek (perhaps somewhat too far) and into Spirit Lake. Also as observed, thick model deposits occur in the main valley around the break in slope at Maratta Creek, while to the west, the deposits thin, being confined to the valley floor. Overall, the reproduction of observed deposit thickness is quite satisfactory.

Fig. 13 shows the final deposit distribution by block and unit. To reproduce observations, the selected basal friction coefficients in Table 1 assured that the matrix-rich facies west of the slope break originates almost exclusively from the lower units in the pre-collapse stratigraphy. Particles from all three blocks end up in the matrix-rich facies area, although Block 3 particles are proportionately more abundant than their overall proportion, and Block 1 and 2 particles less abundant. Other observed lithological features reproduced by the model include the dominance of blocks from the upper unit in the spillover area at the eastern end of Johnston Ridge and the tendency for the upper-unit particles that failed to pass over the ridge to concentrate immediately at its base.

Seismic Source Model. Columns in Fig. 14 graph mean acceleration (left-hand panel), velocity (centre panel), and displacement (right-hand panel) histories for the landslide of Fig. 11. The velocity history shows the initial northward and subsequent westward movement of the landslide coinciding with a quasi-sinusoidal variation in north–south acceleration. Quasi-sinusoidal behaviour contrasts the prediction of the simple block-sliding model of Fig. 1 (bottom panel). The difference reflects the complexity of real landslides

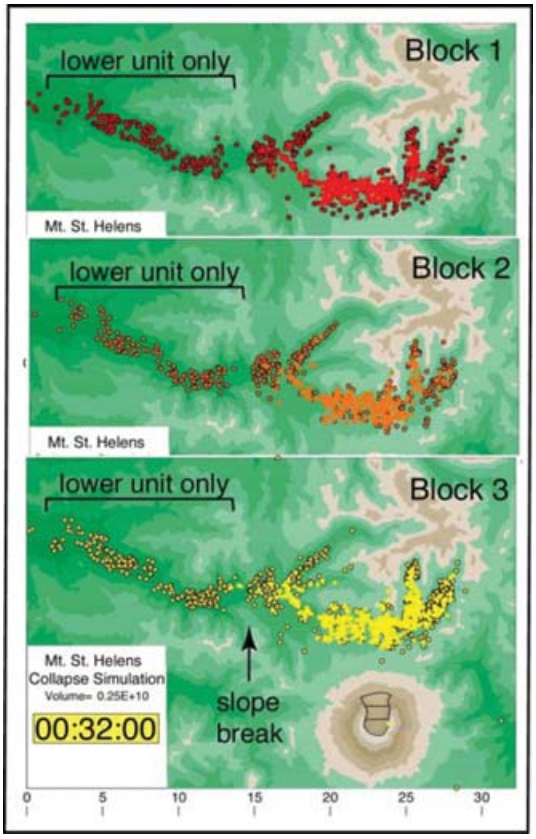

Figure 13. Final deposit distribution by block and unit. In the Mount Saint Helens deposit, only the deeper water-saturated units within the landslide are observed in the further reaches of the slide. In the simulation, these units are given a lower coefficient of basal friction (see Table 1).

moving over real topography. The 4 min duration of the main acceleration signal corresponds to the observed ∼250 s period found in the teleseismic waves. Note too, the significant energy in the 30–60 s period band for $t > 4$ min. Likely, these components parent the short-period seismic waves identified by Malone *et al.* (1981) and Burger & Langston (1985). Short-period variations in mean acceleration, especially in the east–west direction, remain significant to $t = 500$ s, consistent with the duration of the short-period seismic records.

Three distinct acceleration pulses seen in the north–south acceleration history correspond to the release of Blocks 1, 2 and 3 at 30 s intervals. Peak average north–south acceleration reaches about 0.1 g. Using eq. (6) and assuming a slide mass of $M = (2 \times 10^3\,\mathrm{kg\,m^{-3}})(2.5 \times 10^9\,\mathrm{m^3}) = 5 \times 10^{12}$ kg, the Mount Saint Helens slide model puts a peak force of 5×10^{12} N on the Earth's surface. Inversions of seismic records (Emily Brodsky, private communication, 2005) prefer a somewhat larger force of 8×10^{12} N; however, we do not believe that this is a serious discrepancy—peak model forces increase by about 50 per cent if block release intervals drop from 30 to 25 s, within the uncertainty in timings of initial movement of the landslide (Voight 1981). Detailed matches between the model force and inferred seismic force histories are left to a separate paper.

5.3 Evaluation of the landslide model

The success of granular kinematic landslide models lies in their ability to maintain overall consistency with observed deposits while

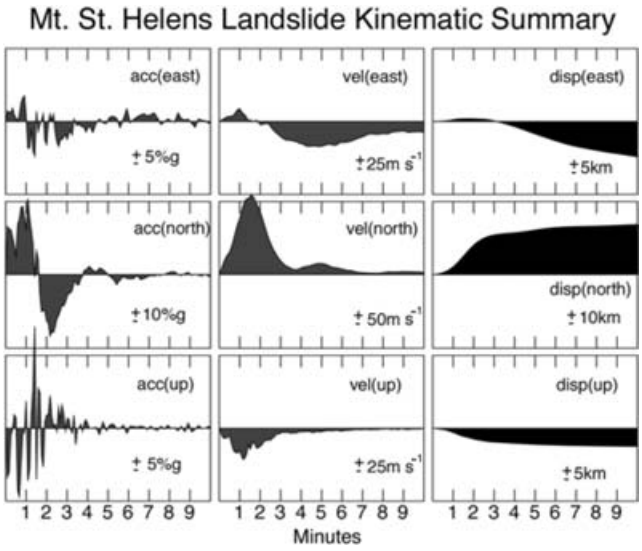

Figure 14. Mean kinematic history of the Mount Saint Helens landslide model of Fig. 11. Acceleration (left-hand panel), velocity (middle panel) and displacement (right-hand panel) histories for the first 10 min of motion. Predominant acceleration signal is a nearly sinusoidal, 4-min-period, north–south directed pulse.

simultaneously satisfying constraints from eyewitness and seismic data. In the case here, we enforced some agreements such as the timed releases of Blocks 1, 2 and 3. Other agreements were made indirectly, such as choosing μ to reproduce known runout distances in the two parts of the deposit and ν such that most particles deflected against Johnston Ridge while a fraction passed up and over. Even so, other consistencies exist that were not dictated directly or indirectly, and are given as follows.

(1) The correct proportions of material deflected east into Spirit Lake and down-valley to the west. More generally, the model thickness distribution closely matches the observed thickness distribution throughout the deposit.

(2) Of the particles that climb on to Johnston Ridge, some emplace on the crest and on the eastern spillover area, others slump back into the valley to the south. This matches the occurrence of small debris avalanche deposits on the ridge crest, the rather more substantial deposits in the spillover, and the evidence for slumping of landslide blocks back down the south face of the ridge to form the terrace features at its foot.

(3) Many more particles enter then exit South Coldwater Creek than deposit in it. This conforms with the extensive bedrock scouring of the creek walls and the small amount of debris avalanche material on its floor.

(4) The model agrees with the kinematic constraints provided by the seismic record, in terms of the timing of the impact of the debris avalanche into Johnston Ridge, the consequent reversal of the north–south acceleration, and the net forces imposed on the Earth's surface.

6 APPLICATIONS AND EXTENSIONS

Because of the simplicity of our granular kinematic landslide model in comparison to its level of success, we believe that it may find many applications and extensions.

Rapid hazard analysis and mitigation. Often, mitigation of landslide hazard requires rapid assessment of potential debris damage zones. A typical situation might ask, 'within plausible frictional behaviours, could the unstable rock mass up there avalanche with sufficient speed to climb that ridge and threaten the town on the other side?' Although full mechanical simulations of fluid-like flows might supply answers, they make far more demands on computational facilities than available in time-critical situations. In contrast, 'laptop computer' scale granular kinematic calculations like these offer rapid guidance.

Studies of other gravitationally driven flows. We see no reason that diverse gravitationally driven processes like snow avalanches, pyroclastic flows and submarine landslides could not be described within this particulate kinematic framework by allowing subtly different mechanisms of movement and friction. In fact, we have already successfully applied the method to the collapse of oceanic island volcanoes and stratovolcanoes, to failures on continental slopes and submarine canyons, and even to tsunami run up using a granular ocean (Ward & Day 2005). Applications to submarine landslides are particularly exciting because of the tsunamigenic potential of underwater mass movements associated with volcano collapses. Imagine a Mount Saint Helens-like collapse of an oceanic island volcano. The extent of tsunami spawned from the collapse depends on the velocity, direction and thickness of the debris flow and the local water depth. Granular kinematic landslide models provide all of the information needed for tsunami simulation.

Enhanced discrimination of earthquake and landslide seismic signals. Certain landslides generate seismic waves more efficiently than others. Granular landslide models present a perfect forum to explore the conditions required for efficient seismic wave production and to advance seismic discrimination of earthquakes from landslides. Moreover, because granular kinematic models suitably describe generation conditions for both seismic and tsunami waves, they speak towards the potential for discriminating tsunami generating slides from non-hazardous ones based on their seismic signatures.

7 FINAL THOUGHT

In this article, using a mechanical model hardly more complex than a sliding block, we have reproduced the overall geometry of the Mount St Helens debris avalanche deposit and satisfied the available kinematic constraints. Standard landslide observations have been played out seemingly, and are incapable of resolving additional parameters in more sophisticated first-principle models. Fresh observational constraints on landslide mechanics lay in detailed analysis of debris avalanche deposit structures, lithological differentiation, and internal deformation down to the clast scale. Especially telling are studies of exposed basal sliding surfaces where direct evidence of mechanical history remain etched in the rock fabric. Detailed field work prototyped by Glicken's monumental effort at Mount St Helens is a prerequisite for further understanding of large landslide events.

ACKNOWLEDGMENTS

Jon Major introduced us to the Mount Saint Helens debris avalanche deposits during a field visit in 2004 July. We are indebted to him for sharing his knowledge. We are also grateful to Gary Hoffmann, Amelia Lyons, Eugene Morgan, Lee Murai and Eli Silver for discussions, then and subsequently. This work forms part of a study of volcano collapses and debris avalanche deposits in island arcs (NSF OCE-0327004).

REFERENCES

Belousov, A., Belousova, M. & Voight, B., 1999. Multiple edifice failures, debris avalanches and associated eruptions in the Holocene history of Shiveluch volcano, Kamchatka, Russia, *Bull. Volc.,* **61,** 324–342.

Brodsky, E.E., Gordeev, E. & Kanamori, H., 2003. Landslide basal friction as measured by seismic waves, *Geophys. Res. Lett.,* **30**(24), 2236, doi:10.1029/2003GL018485,2003.

Burger, R. & Langston, C.A., 1985. Source mechanism of the May 18, 1980, Mount St. Helens Eruption From Regional Surface Waves, *J. geophys. Res.,* **90,** 7653–7664.

Cooke, R.J.S., 1981. Eruptive history of the volcano at Ritter Island, in *Cooke-Ravian Volume of Volcanological Papers*, Vol. 10, pp. 115–123, ed. Johnson, R.W., Geological Survey of Papua New Guinea Memoir.

Dahlen, F., 1993. Single force representation of shallow landslide sources. *Bull. seism. Soc. Am.,* **83,** 130–143.

Day, S.J., 1996. Hydrothermal pore fluid pressure and the stability of porous, permeable volcanoes, in *Volcano instability on the Earth and other planets*, Vol. 110, pp. 77–93, eds McGuire, W.J., Jones, A.P. & Neuberg, J., Geological Society of London Special Publication.

Denlinger, R.P. & Iverson, R.M., 2004. Granular avalanches across irregular three-dimensional terrain: 1. Theory and computation, *J. geophys. Res.,* **109,** F01014, doi:10.1029/2003JF000085.

Elsworth, D. & Day, S.J., 1999. Flank collapse triggered by intrusion: the Canarian and Cape Verde archipelagoes, *Jl Volc. Geotherm. Res.,* **94,** 323–340.

Erismann, T.H. & Abele, G., 2001. *Dynamics of Rockslides and Rockfalls*, Publ. Springer-Verlag, Berlin.

Evans, S.G., Clague, J.J., Woodsworth, G.J. & Hungr, O., 1989. The Pandemonium Creek Rock Avalanche, British Columbia, *Canadian Geotechnical Journal,* **26,** 427–446.

Fisher, R.V., Glicken, H.X. & Hoblitt, R.P., 1987. May 18, 1980, Mount St. Helens Deposits in South Coldwater Creek, Washington, *J. geophys. Res.,* **92,** 10 267–10 283.

Fritz, H., 2002. Initial phase of landslide generated impulse waves. *Mitteilungen der Versuchsanstalt fur Wasserbau, Hydrologie und Glaziologie*, ETH Zurich 178. 254 pp.

Glicken, H.X., 1996. *Rockslide—Debris Avalanche of May 18, 1980, Mount St. Helens Volcano*, United States Geological Survey Open File Report, Washington, 96–677.

Hampton, M.A., Karl, H.A. & Murray, C.J., 2002. Acoustic profiles and images of the Palos Verdes margin: Implications concerning deposition from the White's Point outfall, *Continental Shelf Research,* **22,** 841–857.

Harbitz, C.B., 1992. Model simulations of tsunamis generated by the Storegga Slides, *Marine Geology,* **105,** 1–21.

Heim, A., 1932. *Burgsturz und Menschenleben*, Publ. Fretz and Wasmuth, Zurich. 218 pp.

Heim, A., 1882. Der Bergsturz von Elm, *Zeitschrift der Deutschen Geologischen Gesellschaft* **34,** 74–115.

Heinrich, P., Boudon, G., Komarowski, J.C., Sparks, R.S.J., Herd, R. & Voight, B., 2001. Numerical simulation of the December 1997 debris avalanche in Montserrat, Lesser Antilles, *Geophys. Res. Lett.,* **28,** 2529–2532.

Hsu, K., 1975. On sturzstroms—catastrophic debris streams generated by rockfalls, *Geol. Soc. Am. Bull.,* **86,** 129–140.

Hubbert, M.K. & Rubey, W.W., 1959. Role of fluid pressure in mechanics of overthrust faulting. I: Mechanics of fluid—filled porous solids and its application to overthrust faulting, *Geol. Soc. Am. Bull.,* **70,** 115–166.

Iverson, R.M., Logan, M. & Denlinger, R.P., 2004. Granular avalanches across irregular terrain: 2. Experimental tests, *J. geophys. Res.,* **109,** F01015, doi: 10.1029/2003JF000084.

Johnson, R.W., 1987. Large-scale volcanic cone collapse: the 1888 slope failure of Ritter volcano, *Bull. Volc.,* **49,** 669–679.

Kanamori, H. & Given, J.W., 1982. Analysis of long-period seismic waves excited by the May 18, 1980 eruption of Mount St. Helens—a terrestrial monopole?, *J. geophys. Res.,* **89,** 1856–1866.

Laberg, J.S. & Vorren, T.O., 2000. The Traenadjupet Slide, offshore Norway—morphology, evacuation and triggering mechanisms, *Marine Geology,* **171,** 95–114.

Le Friant, A., Heinrich, P., Deplus, C. & Boudon, G., 2003. Numerical simulation of the last flank-collapse event of Montagne Pelee, Martinique, Lesser Antilles, *Geophys. Res. Lett.,* **30**(2), 1034, doi:10.1029/2002GL015903.

Lima, A.R., Moukarzel, C.F., Grosse, I. & Penna, T.J.P., 2000. Sliding blocks with random friction and absorbing random walks, *Physical Review E,* **61,** 2267–2271.

Lipman, P.W. & Mullineaux, D.R., (eds). 1981. *The 1980 Eruptions of Mount St. Helens*, United States Geological Survey Professional Paper, Washington, 1250.

Malone, S.D., Endo, E.T., Weaver, C.S. & Ramey, J.W., 1981. Seismic monitoring for eruption prediction, in *The 1980 Eruptions of Mount St. Helens, Washington*, Vol. 1250, pp. 803–813, eds Lipman, P.W. & Mullineaux, D.R., United States Geological Survey Professional Paper.

McEwen, A.S. & Malin, M.C., 1989. Dynamics of Mount St. Helens' 1980 Pyroclastic flows, rockslide-avalanche, lahars and blast, *J. Volc. Geotherm. Res.,* **37,** 205–231.

Miller, D.J., 1960. *Giant Waves in Lituya Bay, Alaska,* US Geological Survey Professional Paper 354-C, US Government Printing Office, Washington, DC.

Normark, W.R., McGann, M. & Slitter, R., 2004. Age of Palos Verdes submarine debris avalanche, southern California, *Marine Geology,* **203,** 247–259.

Norris, R.D., 1994. Seismicity of Rockfalls and Avalanches at Three Cascade Range Volcanoes: Implications for Seismic Detection of Hazardous Mass Movements, *Bull. seism. Soc. Am.,* **84,** 1925–1939.

Pevear, D.R., Dethier, D.P. & Frank, D., 1982. Clay minerals in the 1980 deposits from Mount St. Helens, *Clays and Clay Minerals,* **30,** 241–252.

Plafker, G. & Ericksen, G.E., 1978. Nevados Huascaran avalanches, Peru, in *Rockslides and Avalanches I: Natural Phenomena*, pp. 277–314, ed. Voight, B.. Publ. Elsevier, Amsterdam.

Pollet, N. & Schneider, J.-L.M., 2004. Dynamic disintegration processes accompanying transport of the Holocene Flims sturzstrom (Swiss Alps), *Earth planet. Sci. Lett.,* **221,** 433–448.

Pouliquen, O., 1999. Scaling laws in granular flows down rough inclined planes, *Physics of Fluids,* **11,** 542–548.

Savage, S.B. & Hutter, K., 1989. The motion of a finite mass of granular material down a rough incline, *Journal of Fluid Mechanics,* **199,** 177–215.

Shreve, R.L., 1968. The Blackhawk Landslide, *Geological Society of America Special Paper*, **108,** 47 pp.

Sousa, J. & Voight, B., 1995. Multiple-pulsed debris avalanche emplacement at Mount St. Helens in 1980: Evidence from numerical continuum flow simulations, *J. Volc. Geotherm. Res.,* **66,** 227–250.

Siebert, L., Glicken, H. & Ui, T., 1987. Volcanic hazards from Bezymianny and Bandai-type eruptions, *Bull. Volc.,* **49,** 435–459.

Ui, T., 1983. Volcanic dry avalanche deposits—Identification and comparison with non-volcanic debris stream deposits, *J. Volc. Geotherm. Res.,* **18,** 135–160.

Voight, B., 1981. Time scale for the first moments of the May 18 eruption, in *The 1980 Eruptions of Mount St. Helens, Washington*, Vol. 1250, pp. 69–86, eds Lipman, P.W. & Mullineaux, D.R., United States Geological Survey Professional Paper.

Voight, B., Janda, R.J., Glicken, H.X. & Douglass, P.M., 1983. Nature and mechanics of the Mount St. Helens rockslide-avalanche of 18 May 1980. *Geotechnique,* **33,** 243–273.

Wadge, G., Francis, P.W. & Ramirez, C.F., 1995. The Socompa collapse and avalanche event, *J. Volc. Geotherm. Res.,* **66,** 309–366.

Ward, S.N. & Day, S., 2005. Tsunami Thoughts, *Recorder—Journal of the Canadian Society of Exploration Geophysists*, December 2005, 38–44.

APPENDIX A: CALCULATION OF $\hat{\mathbf{n}}(\mathbf{r})$, $\hat{\mathbf{s}}(\mathbf{r})$ AND $K = -[\hat{\mathbf{v}}\hat{\mathbf{v}}{:}\nabla\hat{\mathbf{n}}(\mathbf{r})]$

With $\hat{\mathbf{x}}$, $\hat{\mathbf{y}}$ and $\hat{\mathbf{z}}$, directions being east, north and up, let $T(x, y)$ be the topographic elevation at (x, y). The vector

$$\mathbf{r}(x, y) = (x\hat{\mathbf{x}}, y\hat{\mathbf{y}}, T(x, y)\hat{\mathbf{z}}),$$

then, locates points on the ground surface. All vectors parallel to the surface tangent plane at **r** include

$$\mathbf{v}(a,b) = \left(a\hat{\mathbf{x}},\ b\hat{\mathbf{y}},\ \begin{bmatrix} (\partial T/\partial x)|_{\mathbf{r}}\, a \\ +\,(\partial T/\partial y)|_{\mathbf{r}}\, b \end{bmatrix} \hat{\mathbf{z}} \right). \tag{A1}$$

Thus, a normal vector to the surface there would be

$$\begin{aligned} \mathbf{n}(\mathbf{r}) &= (-\,(\partial T/\partial x)|_{\mathbf{r}}\,\hat{\mathbf{x}},\ -\,(\partial T/\partial x)|_{\mathbf{r}}\,\hat{\mathbf{y}},\ \hat{\mathbf{z}}) \\ &= -\nabla T(x,y) + \hat{\mathbf{z}}, \end{aligned} \tag{A2}$$

because $\mathbf{n}(\mathbf{r}) \bullet \mathbf{v}\,(a,b) = \mathbf{0}$. The unit normal to the surface at **r** is

$$\hat{\mathbf{n}}(\mathbf{r}) = \frac{-\nabla T(x,y) + \hat{\mathbf{z}}}{\sqrt{1 + \nabla T(x,y) \bullet \nabla T(x,y)}}. \tag{A3}$$

From eq. (1), a downslope vector in the tangent plane would be

$$\begin{aligned} \mathbf{s}(\mathbf{r}) &= -\mathbf{v}(\,(\partial T/\partial x)|_{\mathbf{r}}\,,\,(\partial T/\partial y)|_{\mathbf{r}}) \\ &= -\nabla T(x,y) - \hat{\mathbf{z}}\,(\nabla T(x,y) \bullet \nabla T(x,y)) \\ &= \frac{-\hat{\mathbf{z}} + [\hat{\mathbf{z}} \bullet \hat{\mathbf{n}}(\mathbf{r})]\hat{\mathbf{n}}(\mathbf{r})}{[\hat{\mathbf{z}} \bullet \hat{\mathbf{n}}(\mathbf{r})]^2}. \end{aligned}$$

The last step results from eqs (A2) and (A3) and can be written as

$$-\nabla T(x,y) = \frac{\hat{\mathbf{n}}(\mathbf{r})}{(\hat{\mathbf{z}} \bullet \hat{\mathbf{n}}(\mathbf{r}))} - \hat{\mathbf{z}}.$$

The unit downslope vector at **r** is

$$\hat{\mathbf{s}}(\mathbf{r}) = \frac{-\hat{\mathbf{z}} + (\hat{\mathbf{z}} \bullet \hat{\mathbf{n}}(\mathbf{r}))\,\hat{\mathbf{n}}(\mathbf{r})}{\sqrt{1 - (\hat{\mathbf{z}} \bullet \hat{\mathbf{n}}(\mathbf{r}))^2}}. \tag{A4}$$

From eq. (A2)

$$\begin{aligned} \nabla\mathbf{n}(\mathbf{r}) &= -\nabla\nabla T(x,y) \\ &= -\begin{bmatrix} \hat{\mathbf{x}}\hat{\mathbf{x}}\ (\partial^2 T/\partial x^2)\big|_{\mathbf{r}} \\ +(\hat{\mathbf{x}}\hat{\mathbf{y}} + \hat{\mathbf{y}}\hat{\mathbf{x}})\ (\partial^2 T/\partial x \partial y)\big|_{\mathbf{r}} \\ +\hat{\mathbf{y}}\hat{\mathbf{y}}\ (\partial^2 T/\partial y^2)\big|_{\mathbf{r}} \end{bmatrix}, \end{aligned} \tag{A5}$$

because the particle velocities are assumed to always lie in the tangent plane $\hat{\mathbf{v}} \bullet \hat{\mathbf{n}}(\mathbf{r}) = \mathbf{0}$ and

$$\begin{aligned} \hat{\mathbf{v}} \bullet \nabla\hat{\mathbf{n}}(\mathbf{r}) &= \frac{\hat{\mathbf{v}} \bullet \nabla\mathbf{n}(\mathbf{r})}{\sqrt{1 + \nabla T(x,y) \bullet \nabla T(x,y)}} \\ &= (\hat{\mathbf{z}} \bullet \hat{\mathbf{n}}(\mathbf{r}))\ \hat{\mathbf{v}} \bullet \nabla\mathbf{n}(\mathbf{r}). \end{aligned}$$

The centripetal force term is computed by

$$\begin{aligned} K &= -[\hat{\mathbf{v}}\hat{\mathbf{v}}{:}\nabla\hat{\mathbf{n}}(\mathbf{r})] \\ &= (\hat{\mathbf{z}} \bullet \hat{\mathbf{n}}(\mathbf{r}))\ [\hat{\mathbf{v}}\hat{\mathbf{v}}{:}\nabla\nabla T(x,y)]. \end{aligned} \tag{A6}$$

Eqs (A3)–(A6) provide all that is needed to evaluate accelerations (1), given topography and particle velocity

APPENDIX B: QUICKTIME MOVIES

Readers with access to the World Wide Web can view Quicktime movie simulations of the Mount Saint Helens landslide here:
http://es.ucsc.edu/∼ward/msh_norm.mov
http://es.ucsc.edu/∼ward/msh_colors.mov
http://es.ucsc.edu/∼ward/msh_colors_slow.mov
http://es.ucsc.edu/∼ward/msh_blob.mov